

# Silicon dual-ring modulator

Qianfan Xu\*

Department of Electrical and Computer Engineering, Rice University, 6100 Main St. MS-366, Houston, TX 77005  
qianfan@rice.edu

**Abstract:** A silicon electro-optic modulator based on coupled microring resonators is proposed. The dual-ring modulator has wide optical bandwidth, high extinction ratio and low insertion loss. A simple integrated circuit connecting the two rings allows for fast modulation speed of >40 Gbit/s. This device has both improved optical and electrical performance over a single-ring modulator. The dual-ring modulator can provide a feedback signal for active control of the modulation wavelength.

©2009 Optical Society of America

**OCIS codes:** (130.3120) Integrated optics devices; (230.2090) Electro-optical devices; (250.5300) Photonic integrated circuits

---

## References and links

1. J. Ahn, M. Fiorentino, R. Beausoleil, N. Binkert, A. Davis, D. Fattal, N. Jouppi, M. McLaren, C. Santori, R. Schreiber, S. Spillane, D. Vantrease, and Q. Xu, "Devices and architectures for photonic chip-scale integration," *Appl. Phys., A Mater. Sci. Process.* **95**(4), 989–997 (2009).
2. L. Zhou, S. Djordjevic, R. Proietti, D. Ding, S. Yoo, R. Amirtharajah, and V. Akella, "Design and evaluation of an arbitration-free passive optical crossbar for on-chip interconnection networks," *Appl. Phys., A Mater. Sci. Process.* **95**(4), 1111–1118 (2009).
3. Q. Xu, B. Schmidt, S. Pradhan, and M. Lipson, "Micrometre-scale silicon electro-optic modulator," *Nature* **435**(7040), 325–327 (2005).
4. Q. Xu, S. Manipatruni, B. Schmidt, J. Shakya, and M. Lipson, "12.5 Gbit/s carrier-injection-based silicon microring silicon modulators," *Opt. Express* **15**(2), 430–436 (2007).
5. Q. Xu, B. Schmidt, J. Shakya, and M. Lipson, "Cascaded silicon micro-ring modulators for WDM optical interconnection," *Opt. Express* **14**(20), 9431–9435 (2006).
6. W. M. J. Green, M. J. Rooks, L. Sekaric, and Y. A. Vlasov, "Ultra-compact, low RF power, 10 Gb/s silicon Mach-Zehnder modulator," *Opt. Express* **15**(25), 17106–17113 (2007).
7. R. A. Soref, and B. R. Bennett, "Electrooptical effects in silicon," *IEEE J. Quantum Electron.* **23**(1), 123–129 (1987).
8. Q. Xu, S. Sandhu, M. L. Povinelli, J. Shakya, S. H. Fan, and M. Lipson, "Experimental realization of an on-chip all-optical analogue to electromagnetically induced transparency," *Physical Review Letters* **96**, - (2006).
9. Q. Xu, P. Dong, and M. Lipson, "Breaking the delay-bandwidth limit in a photonic structure," *Nat. Phys.* **3**(6), 406–410 (2007).
10. C. Sai Tak, B. E. Little, P. Wugen, T. Kaneko, and Y. Kokubun, "Second-order filter response from parallel coupled glass microring resonators," *IEEE Photon. Technol. Lett.* **11**(11), 1426–1428 (1999).
11. Q. Xu, J. Shakya, and M. Lipson, "Direct measurement of tunable optical delays on chip analogue to electromagnetically induced transparency," *Opt. Express* **14**(14), 6463–6468 (2006).
12. R. F. Pierret, *Semiconductor device fundamentals* (Addison-Wesley, Reading, Mass., 1996).
13. L. Chen, K. Preston, S. Manipatruni, and M. Lipson, "Integrated GHz silicon photonic interconnect with micrometer-scale modulators and detectors," *Opt. Express* **17**(17), 15248–15256 (2009).
14. N. Sherwood-Droz, H. Wang, L. Chen, B. G. Lee, A. Biberman, K. Bergman, and M. Lipson, "Optical 4x4 hitless silicon router for optical networks-on-chip (NoC)," *Opt. Express* **16**(20), 15915–15922 (2008).
15. H.-Y. Ng, M. R. Wang, D. Li, X. Wang, J. Martinez, R. R. Panepucci, and K. Pathak, "4 x 4 wavelength-reconfigurable photonic switch based on thermally tuned silicon microring resonators," *Opt. Eng.* **47**(4), 044601–044608 (2008).
16. L. Chen, N. Sherwood-Droz, and M. Lipson, "Compact bandwidth-tunable microring resonators," *Opt. Lett.* **32**(22), 3361–3363 (2007).
17. Y. A. Vlasov, M. O'Boyle, H. F. Hamann, and S. J. McNab, "Active control of slow light on a chip with photonic crystal waveguides," *Nature* **438**(7064), 65–69 (2005).
18. L. Chen, P. Dong, and M. Lipson, "High performance germanium photodetectors integrated on submicron silicon waveguides by low temperature wafer bonding," *Opt. Express* **16**(15), 11513–11518 (2008).
19. V. R. Almeida, and M. Lipson, "Optical bistability on a silicon chip," *Opt. Lett.* **29**(20), 2387–2389 (2004).
20. J. Sun, C. W. Holzwarth, M. Dahlem, J. T. Hastings, and H. I. Smith, "Accurate frequency alignment in fabrication of high-order microring-resonator filters," *Opt. Express* **16**(20), 15958–15963 (2008).

## 1. Introduction

Electro-optical modulator, the device that converts an electronic signal to an optical signal, is a key component for optoelectronic systems. To build a large-scale integrated optoelectronic system on a silicon chip, like an optical interconnection system for a many-core computer chip [1, 2], compact and high-speed silicon modulators with low power consumption is critical.

Micron-sized silicon modulators based on microring resonators with build-in p-i-n junction have been experimentally demonstrated [3–5]. With an optimized driving circuit, this device has high operation speed [4] and low power consumption. It can be easily integrated in a dense wavelength-division multiplexing (DWDM) interconnection system [1, 5]. The power consumption of the modulator is low when the microring resonator has a sharp resonance (high quality factor  $Q$ ), since a small resonance shift can be converted to a large amplitude modulation. However, a high- $Q$  resonator has a narrow optical bandwidth, which makes it sensitive to fabrication and temperature variations. Since the power consumption of the modulator is directly proportional to the required resonance shift, which is inversely proportional to the sharpness of the resonance, there is a fundamental trade-off between a low power consumption and a wide optical bandwidth. In addition, the experimental demonstration of high-speed modulation using this device relied on an external discrete circuit to create a pre-emphasized driving signal [4, 6].

In this paper, I propose a coupled dual-ring structure which has 3-time wider optical bandwidth of high-quality modulation than the single-ring modulator with the same power consumption (or 3-times less power consumption for the same optical bandwidth). A simple integrated circuit connecting the two rings allows fast modulation ( $> 40$  Gbit/s) without the need for an external pre-emphasis circuit. This dual-ring structure can also provide a feedback signal for thermo-optical control of the operating wavelength.

## 2. Device structure and principle of operation

Figure 1(a) shows the structure of the designed dual-ring modulator. The thick brown lines represent the silicon optical waveguides, which sit on top of a thin (30 to 50 nm thick) silicon slab on a silicon-on-insulator (SOI) wafer. The cross-section of the waveguide is shown in the inset, and is similar to those shown in Ref [3, 6]. The blue and yellow regions represent the areas of the thin silicon slab that is highly doped to p- and n- type respectively. The dope regions and two integrated resistors  $R_S$  are connected by vias and metal wires to form a circuit as the black lines show. There is a  $\text{SiO}_2$  cladding layer with thickness of  $\sim 1$   $\mu\text{m}$  between the silicon waveguide and the metal layer to avoid optical absorption from the metal wires. This device can be fabricated using similar processes as those used in Ref [3, 6].

Figure 1(b) is the equivalent circuit of the device illustrated in Fig. 1(a). Note that all the  $n^+$ -doped regions in Fig. 1(a) are electrically connected by metal wires and form the point  $A$  in the circuit diagram of Fig. 1(b).  $D_1$  and  $D_2$  characterized the p-i-n junctions across the two rings respectively. A serial resistors  $R_C$  is added to each junction to characterize the contact resistance between the metal connections and the doped silicon area. The contact resistances at both sides of the junction are factored in. To obtain a fast modulation,  $R_C$  needs to be much smaller than  $R_S$ .

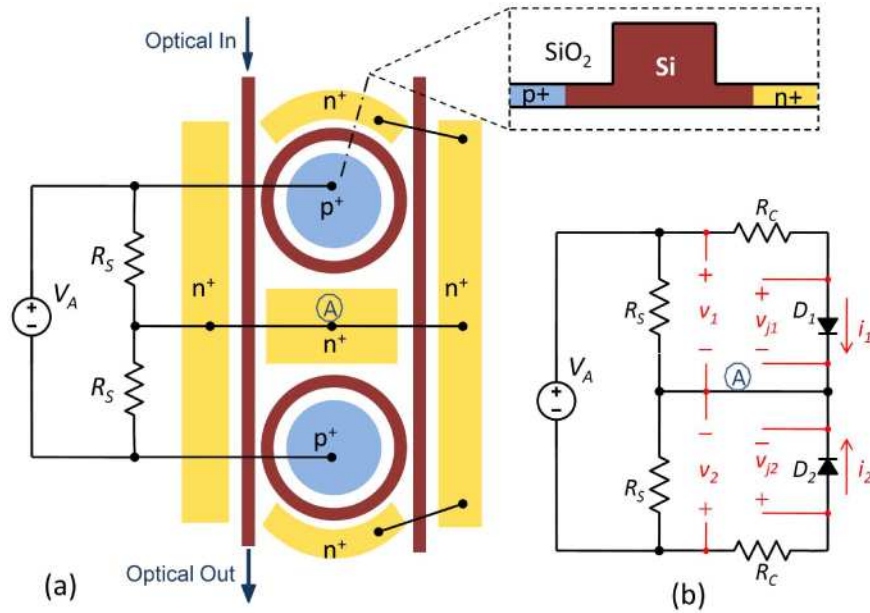


Fig. 1. Diagram of the dual-ring silicon modulator. (a) Top-view of the modulator structure with an overlay of electrical connections. The inset shows the cross-section of the rings. (b) Circuit model of the device.

Under the steady state, if the applied voltage  $V_A$  is positive,  $D_1$  is forward biased and  $D_2$  is reverse biased. The main path of the electrical current goes through  $D_1$  and the lower resistor  $R_S$ . At this state, free carriers (electron-hole pairs) accumulate inside the microring resonator corresponding to  $D_1$ , and blue-shift the resonant wavelength of that microring due to the free-carrier dispersion effect [7]. The amount of electron-hole pairs inside  $D_1$  depends on the forward current through  $D_1$  as

$$N_1 = i_1 \cdot \tau / q \quad (1)$$

where  $\tau$  is the carrier lifetime,  $q$  is the electron charge, and the current  $i_1$  is set by the resistor  $R_S$  as

$$i_1 \approx (V_A - V_{th}) / (R_S + R_C) \approx (V_A - V_{th}) / R_S \quad (2)$$

where  $V_{th}$  is the threshold voltage of the p-i-n diode ( $\sim 0.7$  V). Since the steady-state current required for the modulator is very small, on the order of 0.1 mA, the resistor  $R_S$  can be as high as a few k $\Omega$ , minimizing the steady-state power consumption.

When the applied voltage  $V_A$  switches from positive to negative, the circuit will switch to an opposite state (given the symmetry of the circuit), where carriers are depleted in the reverse-biased  $D_1$  and accumulated in the forward-biased  $D_2$ . The switching process can be very quick since all we need is for the carriers originally accumulated in  $D_1$  to move to  $D_2$  through the low-resistance ( $R_C$ ) path between them. When the new steady state is established, the amount of carriers in  $D_2$  will be the same as that originally in  $D_1$ . As the carriers move from  $D_1$  to  $D_2$ , the resonant wavelengths of the two coupled microrings shift in opposite directions, causing an on-off optical modulation in a certain wavelength range. This is in contrast to a single-ring modulator, where the same carrier movement only causes the resonance of the single ring to shift, resulting in a much narrower optical bandwidth with the same power consumption. This will be analyzed in detail in the next section. Since the modulation operation is accomplished by carriers swinging back and forth between the two

microrings, instead of injecting externally, the modulation speed can be very fast, as will be shown in the detailed electrical analysis in section 4.

### 3. Optical characteristics

The dual-ring resonator structure shown in Fig. 1(a) has a transmission spectrum with a peak in the center of a broader dip [8–10]. The width and height of the central peak depend on the detuning between the two rings, and this characteristic has been used for slowing and stopping of light [9, 11]. Here, the height change of the central peak is used for amplitude modulation purpose.

In this design, I assume that the radii of the two microrings are both  $\sim 5 \mu\text{m}$ , the power coupling coefficient between the microrings and the waveguides are 3.6%, the intrinsic quality factor  $Q_{\text{int}}$  of the two microrings are both 100,000, which is close to what we demonstrated experimentally [3, 9]. Without carrier injection, the resonant wavelengths of the two microring resonators are assumed to be  $\lambda_1 = 1550 \text{ nm}$  and  $\lambda_2 = 1550.35 \text{ nm}$  respectively. Optical modulation is obtained when a number of carriers, which is enough to blue-shift the resonant wavelength of one microring resonator by 0.3 nm, are driven from one ring to the other. When these carriers are in microring  $D_1$ , its resonant wavelength blue-shift to 1549.7 nm, and the optical transmission of the device is shown as the red dashed line in Fig. 2(a). When these carriers are in microring  $D_2$ , its resonant wavelength blue-shift to 1550.05 nm, the detuning between the two microrings reduces to 0.05 nm, and the optical transmission of the device is shown as the blue solid line in Fig. 2(a), where the central transmission peak almost disappears. The central peak would completely disappear if the detuning is further reduced to 0.

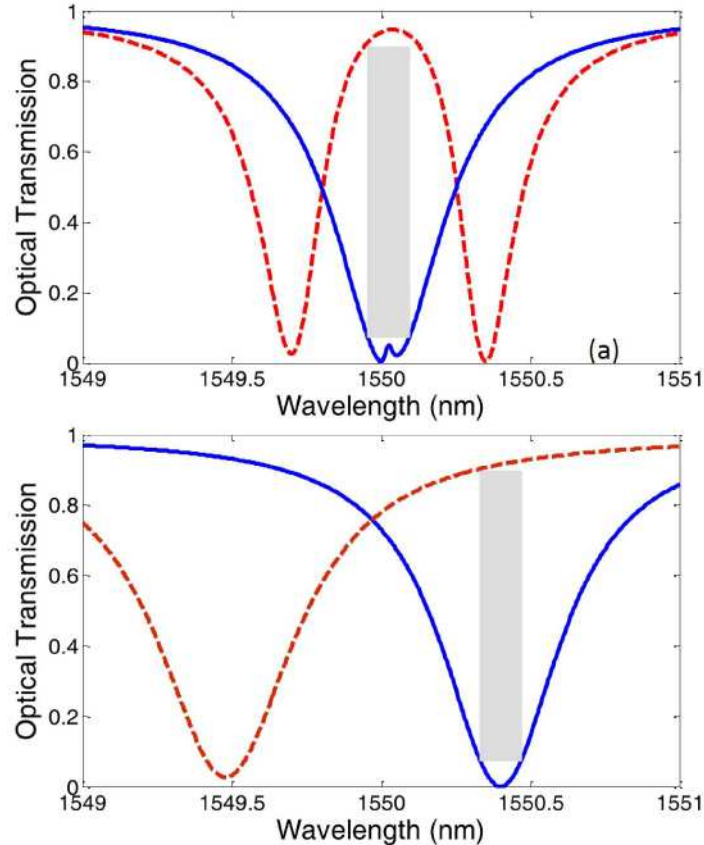


Fig. 2. (a) Transmission spectra of the dual-ring modulator when the carriers are in ring  $D_1$  (red dashed line) and ring  $D_2$  (blue solid line) respectively. (b) Transmission spectra of a single-ring modulator with (red dashed line) and without (blue solid line) carriers in the ring.

For light with wavelength within the gray rectangular area in Fig. 2(a), the ON state has over 90% transmission, corresponding to an insertion loss of less than 0.5 dB; and the OFF state has below 10% transmission, corresponding to an extinction ratio of  $\sim 10$  dB. Here, we define the optical bandwidth of the modulator to be the width of the wavelength region where 10%-90% modulation can be achieved (namely the gray regions in Fig. 2). For the device shown in Fig. 2(a), the optical bandwidth is 0.16 nm, while the resonance tuning necessary to obtain this bandwidth is 0.3 nm. Since the required resonance tuning is proportional to the power consumption, we can define a figure-of-merit (FOM) of the modulator to be the ratio between the optical bandwidth defined above and the required resonance tuning. The FOM equals 0.53 in the dual-ring modulator shown above.

In comparison, Fig. 2(b) shows the transmission spectra of a single-ring modulator with a 5- $\mu\text{m}$  radius. We assume this microring modulator is critically coupled the waveguide and has an ideal Lorentzian line-shape. The gray area in the figure marks the region where 10%-90% modulation can be obtained. The width of this region (the optical bandwidth) is the same as the dual-ring modulator shown in Fig. 2(a), however, the resonance of the microring need to be blue-shifted 0.8 nm to obtain this bandwidth. The FOM (bandwidth/tuning ratio) is thus only 0.17, three times smaller than that of dual-ring modulator shown above. This means, with the same modulation bandwidth and ring parameters, the single-ring modulator requires 3 times more carriers to be moved in and out of the rings than the dual-ring modulator, which corresponds to a 3 times higher power consumption.

Figure 2(a) also shows that, like the single-ring modulators, the dual-ring modulators can be cascaded along a single waveguide to form a dense-wavelength-division-multiplexing (DWDM) modulation system [5]. While the optical transmission changes dramatically around the resonant wavelengths of the microrings, the transmission at wavelength over 1 nm away from the central wavelength is almost constant and close to 100%. If an adjacent wavelength channel is placed 1 nm from the central wavelength of this channel (1550 nm), this modulator will only introduce a small insertion loss of 0.23 dB, and a very low inter-channel interference with only 0.05-dB modulation to the adjacent channel. From Fig. 2(b), one can see that the single-ring modulator with the same bandwidth requires a much larger channel spacing to avoid a significant inter-channel interference.

#### 4. Electrical characteristics

The circuits connecting the dual-ring modulator, as shown in Fig. 1(b), allows fast carrier transfer between the two microrings. To calculate the carrier dynamics, the circuit is modeled by the following equations.

$$dN_1 / dt = i_1 / q - N_1 / \tau \quad (3)$$

$$dN_2 / dt = i_2 / q - N_2 / \tau \quad (4)$$

$$v_{j1} = v_0 \cdot \log[N_1 \cdot q / (I_0 \cdot \tau) - 1] \quad (5)$$

$$v_{j2} = v_0 \cdot \log[N_2 \cdot q / (I_0 \cdot \tau) - 1] \quad (6)$$

$$i_1 = (v_1 - v_{j1}) / R_C \quad (7)$$

$$i_2 = (v_2 - v_{j2}) / R_C \quad (8)$$

$$v_1 - v_2 = V_A \quad (9)$$

$$i_1 + i_2 + v_1 / R_S + v_2 / R_S = 0 \quad (10)$$

Equation (3)-(6) come from the basic property of the two p-i-n junctions [12]. Equation (7)-(10) come from the property of the circuits that connects the two junctions. The currents and voltages in these equations are defined in Fig. 1(b).  $N_1$  and  $N_2$  are the number of electron-hole pairs inside the ring  $D_1$  and ring  $D_2$ , respectively. Note that Eq. (1) is simply the steady-state solution of Eq. (3). For an ideal diode,  $v_0 = kT / q = 0.026$  V, but these junctions are operating partially in the high-level-injection region where  $v_0 = 2kT / q = 0.052$  V. Here, I use the numbers obtained from fitting the experimentally measured I-V curve of a microring modulator, which are  $v_0 = 0.044$  V, and  $I_0 = 0.28$  pA.

The dynamic behavior of the circuit is simulated based on these equations, assuming a non-return-to-zero (NRZ) pseudo-random bit sequence (PRBS  $2^7-1$ ) voltage signal at a bit rate of 40 Gbit/s is applied. In the simulation,  $\tau = 1$  ns;  $R_C = 80$   $\Omega$ , which is achievable according to the experimental result in [6]; and  $R_S = 3$  K $\Omega$ , which gives us the right amount of carriers in the rings. Because Eq. (5) and (6) are highly nonlinear, to help with the convergence of the simulation, we neglected the small reverse-bias currents of the two diodes in the simulation (i.e. assumed  $i_1 = 0$  when  $V_{j1} < 0$  and  $i_2 = 0$  when  $V_{j2} < 0$ ).

Figure 3(a) shows the waveform of the driving signal  $V_A$  which swings between  $\pm 3$  V. Figure 3(b) shows the number of electron-hole pairs in each microring. When the driving voltage changes, most of the carriers are quickly driven from one ring to the other, so that the number of carriers in one ring rises while that in the other ring drops. The transition time is less than 10 ps. However, as evident from the figure, a small portion of carriers are lost in each transition, due to the current that goes through  $R_S$ . After the fast transition, the number of carriers continues to rise to its steady-state value, with a time constant determined by the

carrier lifetime  $\tau$ . Even though the percentage of carrier lost in each transition is small, which is proportional to  $R_C / R_S$ , there is a larger drop in the number of carriers when the transition is more frequent. That creates some variation of the carrier quantities in the rings that depends on the bit patterns. However, this variation in the carrier quantities only has a small effect on modulated optical output, because the optical transmission is not sensitive to small variation of carrier quantity when the transmission is above 90% or below 10%.

The total power consumption of the circuit is calculated from the simulation to be 12 mW at 40 Gbit/s. This corresponds to an energy consumption per bit of 0.3 pJ/bit, which is an order of magnitude smaller than that shown in silicon modulators based on Mach-Zehnder interferometers [6]. Lower energy consumptions have been achieved in single-ring modulators [13] only with sacrifices in optical bandwidth, modulation speed, insertion loss or extinction ratio.

The fast carrier transfer process between the two rings can also be explained as an internal self-limiting pre-emphasis effect. When the applied voltage  $V_A$  changes from positive to negative, the voltage drop on  $D_1$  ( $v_{j1}$ ) remains positive before the carriers are completely depleted [12]. Therefore, most of the negative bias voltage drops on  $D_2$  and its contact resistance, which is a large forward-biasing voltage for  $D_2$  similar to that used in the pre-emphasis scheme [4]. This large forward-biasing voltage results in a fast charging of  $D_2$  and a corresponding fast de-charging of  $D_1$ . After all the carriers in  $D_1$  are depleted,  $D_1$  becomes reversed bias and most of the negative voltage now drops on  $D_1$  instead of  $D_2$ . The fast charging process stopped automatically at this point. The voltage drops and currents through the two junctions are plotted in Fig. 3(c) and (d). We can see a voltage spike immediately following every negative-to-positive transition, similar to what we created in the pre-emphasis scheme [4] to allow fast modulations. This voltage spike drops on the small contact resistance  $R_C$ , and creates the current peaks shown in Fig. 3(d), which is responsible for the quick transfer of carriers between the two rings.

In the theoretical model, the transition time, and thus the modulation bit-rate, are mainly limited by the contact resistance  $R_C$ . The transition time increases linearly with  $R_C$ . In a real device, the transition time is also limited by how fast the electrons and hole can physically move across the junction. This limitation is not considered in the circuit model, and therefore is not reflected in the simulation results. From the saturation speed of electrons and holes in silicon, the time for the carriers to travel across the junction can be less than 10 ps, allowing for a modulation speed over 40 Gbit/s.

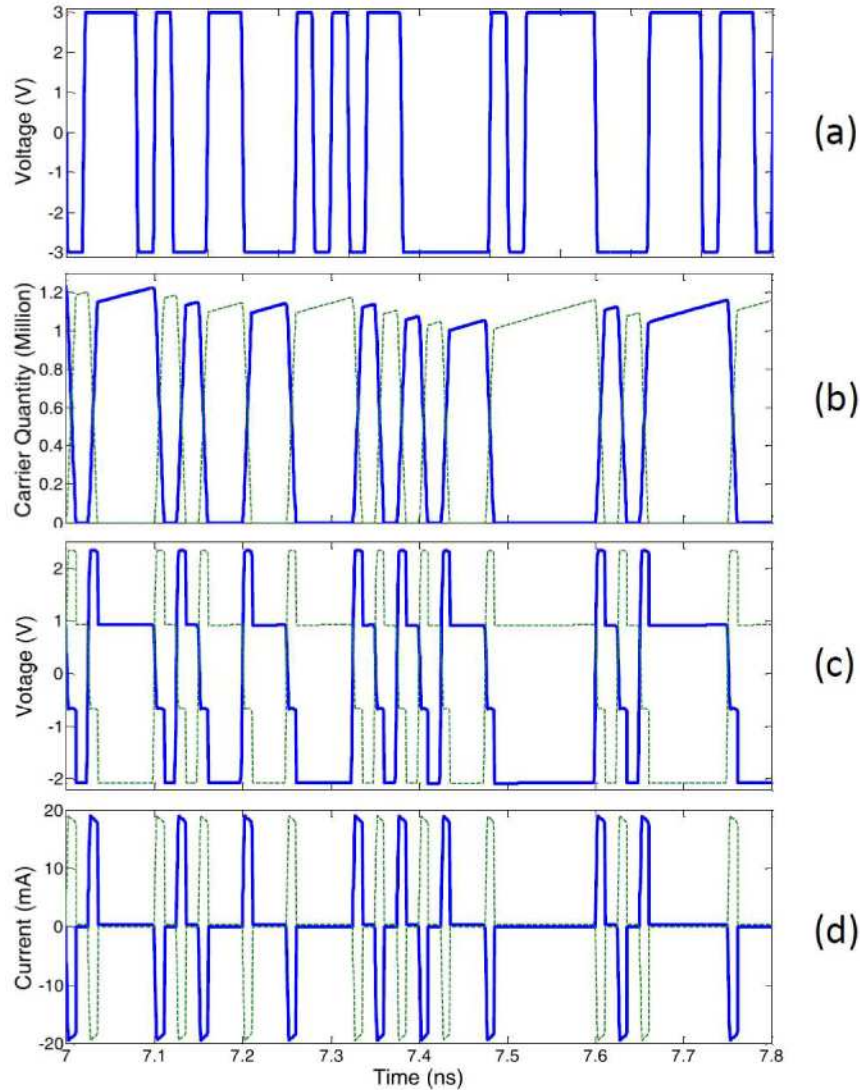


Fig. 3. (a) Waveform of the applied voltage  $V_A$ , which swings between  $\pm 3$  V at 40 Gbit/s. (b) Waveform of the number of electron-holes pairs in the two rings  $N_1$  (blue solid line) and  $N_2$  (green dashed line). (c) Waveform of the voltage  $v_1$  (blue solid line) and  $v_2$  (green dashed line). (d) Waveform of the current  $i_1$  (blue solid line) and  $i_2$  (green dashed line).

## 5. Optoelectronic modulation

As the number of carriers in the two microrings changes, so does the refractive index of silicon forming the ring, due to the free-carrier plasma dispersion effect [7]. The temporal change of refractive index is obtained based on the carrier distribution in the two microrings calculated in the last section (see Fig. 3(b)). This temporal change of refractive index is plugged into a time-domain model of the dual-ring modulator [9], where the output optical power is simulated assuming a cw light at the input. Note that the frequency-domain model used in section 2 to obtain Fig. 2 assumes time-invariant system, therefore cannot strictly apply here, as the characteristic time of the index variation is comparable to the photon lifetime in the device. Figure 4(a) shows the simulated output waveform of the modulator for light with a wavelength of 1550 nm. Figure 4(b) shows the corresponding eye-diagram of the

optical output signal. The eye is clearly open and 10%-90% modulation with transition time  $\sim 10$  ps is achieved.

One can see from the waveform in Fig. 4(a) that a pulse with a transmission higher than 100% appears at each leading edge of the waveform. This is because part of the optical energy is stored in the dual-ring resonator when it is in the OFF state, and released back into the output waveguide when it is switched to the ON state [9], causing the instantaneous output power to be higher than the input power. Similar effect has been observed experimentally in single-ring modulators too [5]. The extra optical power from the energy release does not significantly interfere with modulation operation.

To show the optical bandwidth of the device, Fig. 4(c) shows the eye-diagram at the wavelength of 1549.96 nm and Fig. 4(d) shows the eye-diagram at the wavelength of 1550.08 nm. The bandwidth where 10%-90% modulation can be achieved is thus 0.12 nm. This is slightly less than the 0.16-nm bandwidth measured from Fig. 2(a), because of the temporal dynamics that are not taken into account in the frequency-domain model used to calculate Fig. 2(a), and because of the bit-pattern-dependent variation of charge quantity in the microrings.

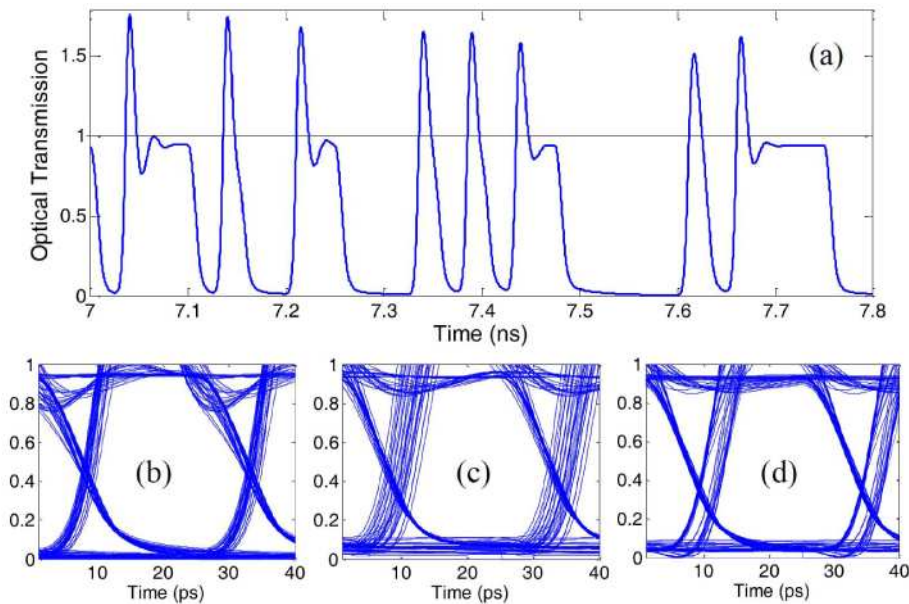


Fig. 4. (a) Waveform of the modulated optical output at  $\lambda = 1550$  nm under the 40-Gbit/s driving signal shown in Fig. 3(a). (b) Eye-diagram of the modulated optical output at  $\lambda = 1550$  nm. (c) Eye-diagram of the modulated optical output at  $\lambda = 1549.96$  nm. (d) Eye-diagram of the modulated optical output at  $\lambda = 1550.08$  nm.

## 6. Feedback signal for thermo-optic control

Even with the improved optical bandwidth, the modulator shown above can only tolerate temperature variation of  $\sim 1$  °C [14], which is below the range of temperature variation in a computer processor. Plus, the exact dimensions of the microrings can vary from die to die and from wafer to wafer, which cause a change in the operational wavelength of each fabricated modulator. To compensate for the environmental temperature variation and fabrication imperfections, an electrical heater with an active feedback control mechanism is likely to be required for each modulator.

Thermo-optic tuning of silicon photonic devices has been demonstrated experimentally with both external and internal heaters [14–17]. However, for a single-ring modulator, it is challenging to obtain a feedback signal to determine whether or not the ring resonance is at the optimal wavelength and to decide the direction of the required tuning, especially while the

modulator is actively operating. One possible approach is to split off a portion of the modulated optical output to analyze the modulation quality. This approach, however, increases the insertion loss of the modulator, and requires high-speed detector and high-speed electronic circuits, which significantly increases the complexity and the power consumption of the system.

The dual-ring modulator proposed here presents a feedback signal that can be extracted with two low-speed detectors, which detect light scattered from the two rings. The power of the scatter light from each ring is linearly proportional to the optical energy inside the ring, which is determined by how far the input wavelength is from the resonant wavelength of the ring. When the input light is at the optimal operating wavelength of the modulator, which is at the center of the two ring resonances, the scattered light from the two rings should be equal. When the wavelength of light is off the center, the ring with resonance closer to the wavelength of light will scatter more light than the other. Therefore the difference between the scattered powers of the two rings indicates which direction to shift the two ring resonances so that the wavelength of light will be centered between them.

This feedback scheme can work even when the device is actively modulating light, since the input wavelength should always be at the center of the two ring resonances, for both on and off state and any transitional state in between. A germanium detector can be integrated [18] on top of each ring to collect its scattering light and measure the power that is averaged by many bit periods. The speed of detector can be on the order of MHz, which only needs to be faster than the  $\mu\text{s}$ -level thermal response time [19]. Because the detector can have relatively long integration time, a small portion of the scattered light is enough to obtain a good signal-to-noise ratio for the feedback signal.

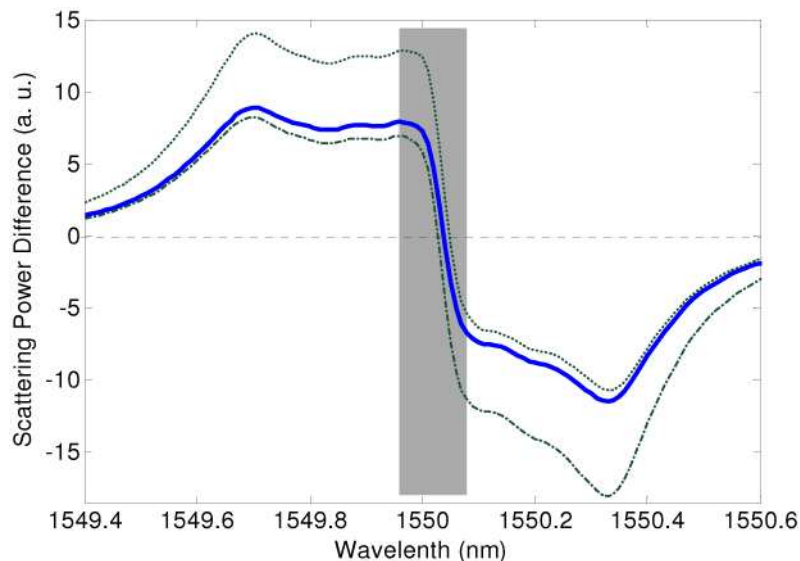


Fig. 5. Difference in the time-averaged scattered optical power (scattered optical power from ring  $D_1$  minus that from ring  $D_2$ ) versus the wavelength of input light when the dual-ring modulator is modulated by the 40-Gbit/s signal shown in Fig. 3(a). Solid line:  $D_1$  and  $D_2$  have the same scattering efficiency. Dot line:  $D_1$  has 50% higher scattering efficiency than  $D_2$ . Dash-dot line:  $D_2$  has 50% higher scattering efficiency than  $D_1$ .

The solid line in Fig. 5 shows the difference in the time-averaged scattered power between the two rings as a function of the wavelength of light. This function is obtained from the optoelectronic simulation assuming the dual-ring modulator is operating at the same condition as that shown in Fig. 4. This curve crosses the zero line within the wavelength range for high-quality modulation (gray area in the figure, between 1549.96 nm and 1550.08 nm) and is

positive on one side and negative on the other side. Therefore, a simple control circuit that heat up the rings more or less depending on the sign of this feedback signal can bring it to zero, thereby keep the input wavelength within the optimal range.

Since the scattering of light is mainly caused by random-distributed side-wall roughness of the rings, the scattering efficiency (the ratio between the scattered optical power and the optical energy inside the ring) may be different for the two rings. This difference, however, would not significantly affect the proposed feedback scheme. To show that, we simulated the feedback signal when the scattering efficiency of ring  $D_1$  is 50% higher than that of  $D_2$  (dotted line in Fig. 5) and when the scattering efficiency of ring  $D_2$  is 50% higher than that of  $D_1$  (dash-dot line in Fig. 5). The assumed large variation of scattering efficiency has little effect on where the feedback signal crosses zero line. Both curves cross the zero line well within the wavelength range for high-quality modulation.

Note that, since the two rings are very close to each other, their temperature difference and their relative dimensional variation are very small [20]. The detuning between the two rings ( $\lambda_2 - \lambda_1$ ) thus has much less variation than the absolute wavelengths of their resonances. Therefore I assumed here that the detuning can be reproduced as designed and does not require active control.

## 7. Summary

In conclusion, I have shown in this paper a dual-ring silicon modulator that has superior optical and electrical performance over the single-ring modulator structure. With the same optical bandwidth for high-quality modulation, the dual-ring modulator consumes 3-times less power than the single-ring modulator with the same ring radius. A simple circuit connecting the two rings allows a fast and self-limiting carrier transfer between the two rings, and a modulation speed over 40 Gb/s can be obtained without an external pre-emphasis scheme that is necessary for the single-ring modulator. With integrated low-speed detectors to collect the scattered light, a feedback signal can be obtained in order to align the operating wavelength of the modulator with the wavelength of input light.